CrossMark

Epitaxial thin-film growth of Ruddlesden–Popper-type $Ba_3Zr_2O_7$ from a $BaZrO_3$ target by pulsed laser deposition

Shariqa Hassan Butt[1] · M. S. Rafique[1] · K. Siraj[1] · A. Latif[1] · Amina Afzal[1] ·
M. S. Awan[2] · Shazia Bashir[3] · Nida Iqbal[4]

Abstract Ruddlesden–Popper $Ba_3Zr_2O_7$ thin films have been synthesized via pulsed laser deposition (PLD) technique. The optimization of deposition parameters in PLD enables the formation of thin film of metastable $Ba_3Zr_2O_7$ phase from $BaZrO_3$ target. In order to see the post-annealing effects on the structural and optical properties, the deposited $Ba_3Zr_2O_7$ thin films were annealed at 500, 600 and 800 °C. X-ray diffraction (XRD) reveals the formation of $Ba_3Zr_2O_7$ phase with tetragonal structure. The changes in the surface of the deposited films were analysed by FE-SEM and AFM. The thin film post-annealed at 500 °C exhibited the best structural, optical and surface properties. Furthermore, the chemical states and chemical composition of the films were determined by X-ray photoelectron spectroscopy (XPS) near the surface. The XPS results show that Ba, Zr and O exist mainly in the form of $Ba_3Zr_2O_7$ Ruddlesden–Popper-type perovskite structure.

✉ Shariqa Hassan Butt
   shariqabutt@gmail.com

1 Laser and Optronics Centre, Department of Physics, University of Engineering and Technology, Lahore 54890, Pakistan

2 Ibn-e-Sina Institute of Science and Technology (ISIT), H-11/4, Islamabad, Pakistan

3 Centre for Advanced Studies in Physics, Government College University, Lahore, Pakistan

4 Medical Devices and Technology Group (MEDITEG), Faculty of Biosciences and Medical Engineering, Universiti Teknologi Malaysia, 81310 Johor Bahru, Johor, Malaysia
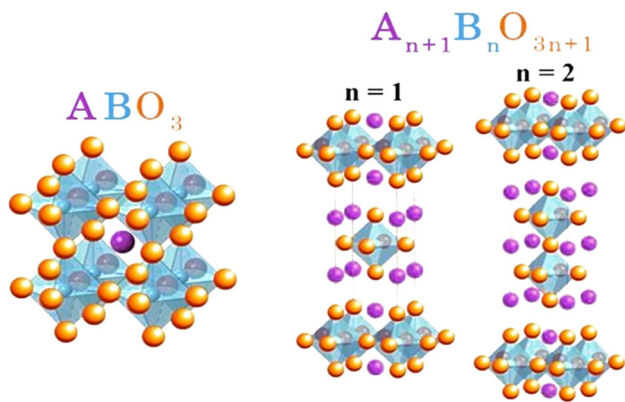
1 Introduction

The main significance of perovskite oxides arises from their compositional diversity. Majority of ABO_3 exhibit distortion from (a) rotation or tilting of BO_6, (b) Jahn–Teller distortion of BO_6 octahedral. The length of A–O and/or B–O bonds gets changed due to this distortion and results in the phase transition from cubic to tetragonal or orthorhombic. ABO_3 perovskite thin films (A = Ba, Ca, Sr, and B = Zr, Ti, etc.) are technologically very important for numerous devices like piezoelectric transducer, transistor, dielectric resonator, dynamic random access memory (DRAMS), magnetic data storage devices, sensors, etc. [1, 2] because of their variable structure and chemical composition [3]. Among the ideal cubic perovskite oxide materials, $BaZrO_3$ being a high-dielectric-constant material has been studied to replace silicon dioxide (SiO_2) gate insulator material of MOS transistors [4]. Theoretical studies support the formation of three phases of barium zirconates $BaZrO_3$, Ba_2ZrO_4 and $Ba_3Zr_2O_7$. Standard Gibb's free energy for the formation of these phases has been reported in literature [5]. $Ba_3Zr_2O_7$ is the most notable example of this distorted structure. Perovskite structures also attract interest due to the ability to incorporate extended defects at high temperatures. Such defects influence the electrical and optical properties, and their controlled incorporation can be used to tune the properties to fulfil the application demands [6]. However, various attempts to prepare $Ba_3Zr_2O_7$ were not successful [5].

$Ba_3Zr_2O_7$ belongs to an example of structural family, derived from perovskite oxides. The Ruddlesden–Popper (RP) family has general formula $A_{n+1}B_nO_{3n+1}$ (Fig. 1) [7] where n corresponds to the number of perovskite layers sandwiched between the double rock-salt layers [8]. These compounds ($n = 1, 2, 3$) belong to tetragonal structure while

Fig. 1 Schematic drawing of the parent ABO_3 $n = \infty$ ($BaZrO_3$, *cubic*), $n = 1$ (Ba_2ZrO_4, *tetragonal*) and $n = 2$ ($Ba_3Zr_2O_7$, *tetragonal*), members of the $Ba_{n+1}Zr_nO_{3n+1}$ RP homologous series

$n = \infty$ compound belongs to cubic structure [9]. These deviated/distorted structures generate asymmetry in the crystal which can promote degeneracy in the atomic orbits. Hence, intermediate states appear in the gap region and band gap energy reduces [2]. Barium zirconate phases exhibit photoluminescence (PL), especially with blue emission. The materials that exhibit blue emissions are very promising for application in high-efficiency blue LEDs, blue laser diode, etc. [10]. $Ba_3Zr_2O_7$ phase has still not been reported in thin-film form. Lower temperature ($T < 500$ °C) is one of the main advantages that offer a potential for the growth of such new compounds and structures [11, 12].

The composition of the films may be changed from that of the target in epitaxial thin-film growth by using pulsed laser deposition (PLD). PLD is a versatile technique having advantage that metastable material or phases like $Ba_3Zr_2O_7$ can be fabricated by optimization of laser or deposition parameters [13]. For example, the lattice constants and electrical properties of the perovskite SrTiO3 thin films could be widely varied by tuning the ablation conditions and the crystal quality. Also phase purity of layered rock-salt $LiCoO_2$ thin films could be tuned by changing the oxygen pressure in addition to the ablation conditions [14].

Here, we report the epitaxial growth of thin films of $Ba_3Zr_2O_7$ from a stoichiometric $BaZrO_3$ target by controlling the deposition parameters. The structural, compositional, morphological and optical properties of novel $Ba_3Zr_2O_7$ thin film have been analysed using XRD, XPS, FE-SEM, AFM and SE, respectively.

2 Experimental set-up

An analytical grade 5 N pure barium zirconate powder has been heat-treated to form pellets to be used as target material for PLD. In order to make a pallet, powder was grounded using agate mortar for 30 min. The fine powder

was then heated in a furnace for 10 h at 500 °C to make sure that no impurities exist in the powder. To homogenise the powder, it was again grounded for 1 h and then pressed using the hydraulic press to form pellet. The pellets were sintered at 900 °C for 18 h to strengthen the pellets and to avoid the voids.

Epitaxial $Ba_3Zr_2O_7$ thin films were fabricated by pulsed laser deposition technique using KrF excimer laser ($\lambda = 248$ nm) operated at a fluence of 1.3 J/cm^2 with repetition rate of 20 Hz. A standard stainless steel chamber was utilized to grow the thin films [15]. $BaZrO_3$ target was kept at a distance of 25 mm from the substrate. N-type single-crystal, silicon (0 0 1) substrate of dimensions $10 \times 10 \times 0.4$ mm^3 was ultrasonically cleaned in the acetic acid followed by acetone. The substrate was kept at a constant temperature of 300 °C during all the depositions. All the films were deposited under high vacuum $\sim 10^{-5}$ - Torr. Post-deposition annealing was carried out at 500, 600 and 800 °C for 2 h in ambient atmosphere.

The structure of the deposited thin films was investigated by X-ray diffractometer (Bruker, D8 discover, Germany) with Cu Kα radiation ($\lambda = 1.5404$ Å). X-ray photoelectron spectroscopy was used to identify the surface stoichiometry and elemental oxidation states of thin-film sample. Field emission scanning electron microscope (JSM-7001F model) and atomic-force microscope (Veeco-CP-II) were used to observe the surface morphology of the films. Optical constants and band gap energy were estimated by using spectroscopic ellipsometry (J. A. Woolam Co. Inc. Various angle spectroscopic ellipsometry).

3 Results

3.1 Structural properties

Figure 2 shows the XRD pattern of all the deposited thin films. The only diffraction peak at 32.95° indicates the formation of crystalline tetragonal structure ($n = 2$ RP structure) of $Ba_3Zr_2O_7$ (0 0 8) plane. The preferred orientation of $Ba_3Zr_2O_7$ is (0 0 8) which is epitaxially grown on Si (0 0 1). The growth of non-stoichiometric (film phase is different from the target ($BaZrO_3$)) tetragonal $Ba_3Zr_2O_7$ thin film which is attributable to the experimental conditions like deposition at low temperature 300 °C, high vacuum ($\sim 10^{-5}$ Torr). The growth might also depend upon the laser parameters, like fluence repetition rate, used for deposition. $Ba_3Zr_2O_7$, a Ruddlesden–Popper (RP) structure, generally crystallizes with tetragonal unit cell. It belongs to the second member of RP family having $n = 2$, which is composed of two infinite BO_6 sheets connected in the c-direction between the rock-salt layers [16]. The c-axis lattice constant of this phase is determined by the formula
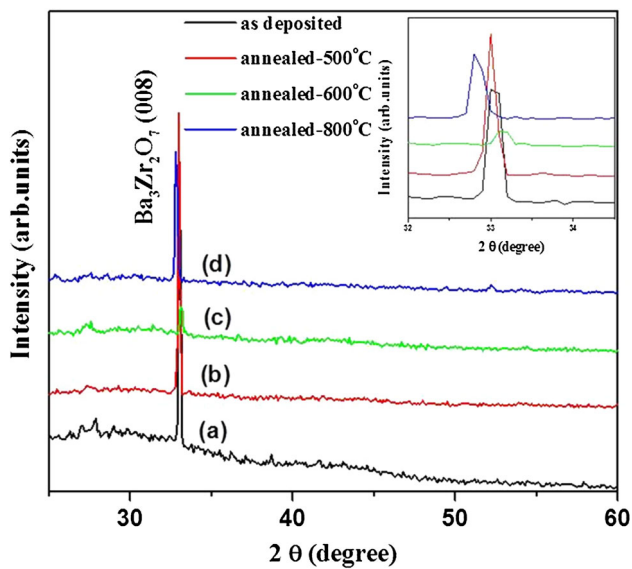
Fig. 2 XRD patterns of $Ba_3Zr_2O_7$ films deposited at 300 °C substrate temperature. *a* as-deposited, *b* annealed at 500 °C, *c* annealed at 600 °C, *d* annealed at 800 °C
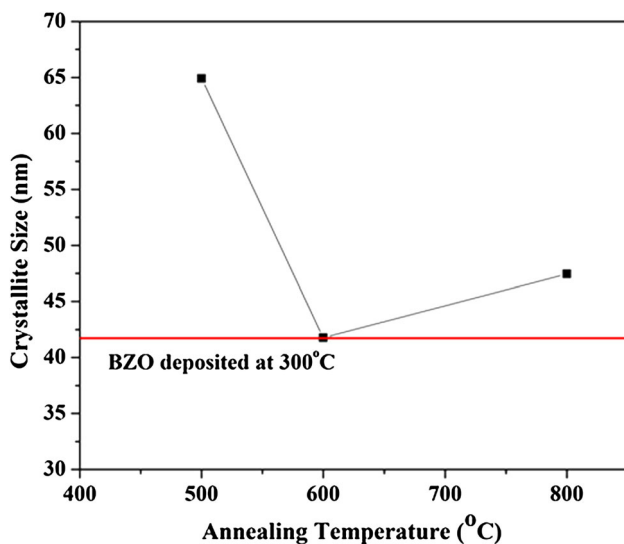

Fig. 3 Variation of crystallite size with the annealing temperature

given in [17] for all the films. The values of c for the as-deposited and annealed films at 500, 600 and 800 °C are 21.67, 21.69, 21.59 and 22.18 Å, respectively. These values are in good agreement with the values of powder phase as in JCPD card (No. 00-02-0131). There is a slight shift in 2θ values with the change in its annealing temperature, shown in the inset of Fig. 2. This peak shifting and asymmetry are indicative of internal stresses and planer defects like non-periodicity in the stacking sequence in c-direction (inter-growth) [18, 19].

The average crystallite size "D" was calculated using Scherrer's formula [20]. Figure 3 shows the variation of

crystallite size with the annealing temperature. Crystallite size was found to be maximum for the film post-annealed at 500 °C. This is due to the increase in the mobility of the atoms with increasing temperature which causes the crystallization of the material resulting in larger grains [21]. Further increase in the annealing temperature shows the decrease in crystallite size. This decrease in crystallite size is attributed to the lattice vibrations that cause permanent distortion in the structure. It appears that 500 °C is the optimum post-annealing temperature for the growth of $Ba_3Zr_2O_7$ thin films. One of the reasons of oxygen deficiency in the films is larger scattering and low sticking coefficient of oxygen atoms with the silicon substrate [22]. The strongest intensity of (0 0 8) peak is obtained for the sample annealed at 500 °C, confirming that the BZO-an-500 has the best crystallinity and largest grain size among the other samples. The crystallite size increases after annealing and decreases on further annealing at higher temperature (600 and 800 °C). This trend has also been reported previously in literature [22].

3.2 XPS analysis

Surface stoichiometry and elemental oxidation states of un-annealed $Ba_3Zr_2O_7$ thin film were studied using XPS by investigating the Ba 3d, Zr 3d and O 1s core level spectra. The binding energies of the spectrum were calibrated by the adventitious carbon C 1s peak centred at $\sim$284.6 eV.

Figure 4 shows survey scan and the core level XPS spectral of Ba_{3d}, Zr 3d and O 1s of the sample. The $Ba_3Zr_2O_7$ film contains Ba, Zr, O and C elements near its surface.

The elemental oxidation states and their relative concentrations were estimated by the relative area under curve of the peaks de-convoluted using Gaussian peak fitting.

Figure 4b shows the core level XPS spectrum of Ba 3d revealing the presence of Ba in different elemental states. A doublet is observed in the XPS spectrum corresponding to the Ba 3d peak as shown in Fig. 4b. The Ba $3d_{5/2}$ and the Ba $3d_{3/2}$ peaks are clearly separated at 780.1 and 796.4 eV to form the expected doublet. The separation between Ba $3d_{5/2}$ and Ba $3d_{3/2}$ peaks is 15.3 eV which is consistent with the character of Ba in $BaTiO_3$ [23].

Figure 4c shows the core level XPS spectrum of Zr 3d. Detailed peak de-convolution shows that the Zr peak is located at 179.34 eV (Zr $3d_{5/2}$), shifted by +0.74 eV relative to pure Zr (178.6 eV) [24].

The de-convoluted peak in Fig. 4d shows the XPS peak of O 1s core level spectrum of O2 implying the presence of oxygen in its different oxidation states. Due to feature of this peak, it was de-convoluted into two peaks, centred at $\sim$530.7 and 532.8 eV. The de-convoluted peak with lower binding energy is associated with the O^{2-} ions in oxygen-deficient regions within the matrix [25, 26]. Hence it
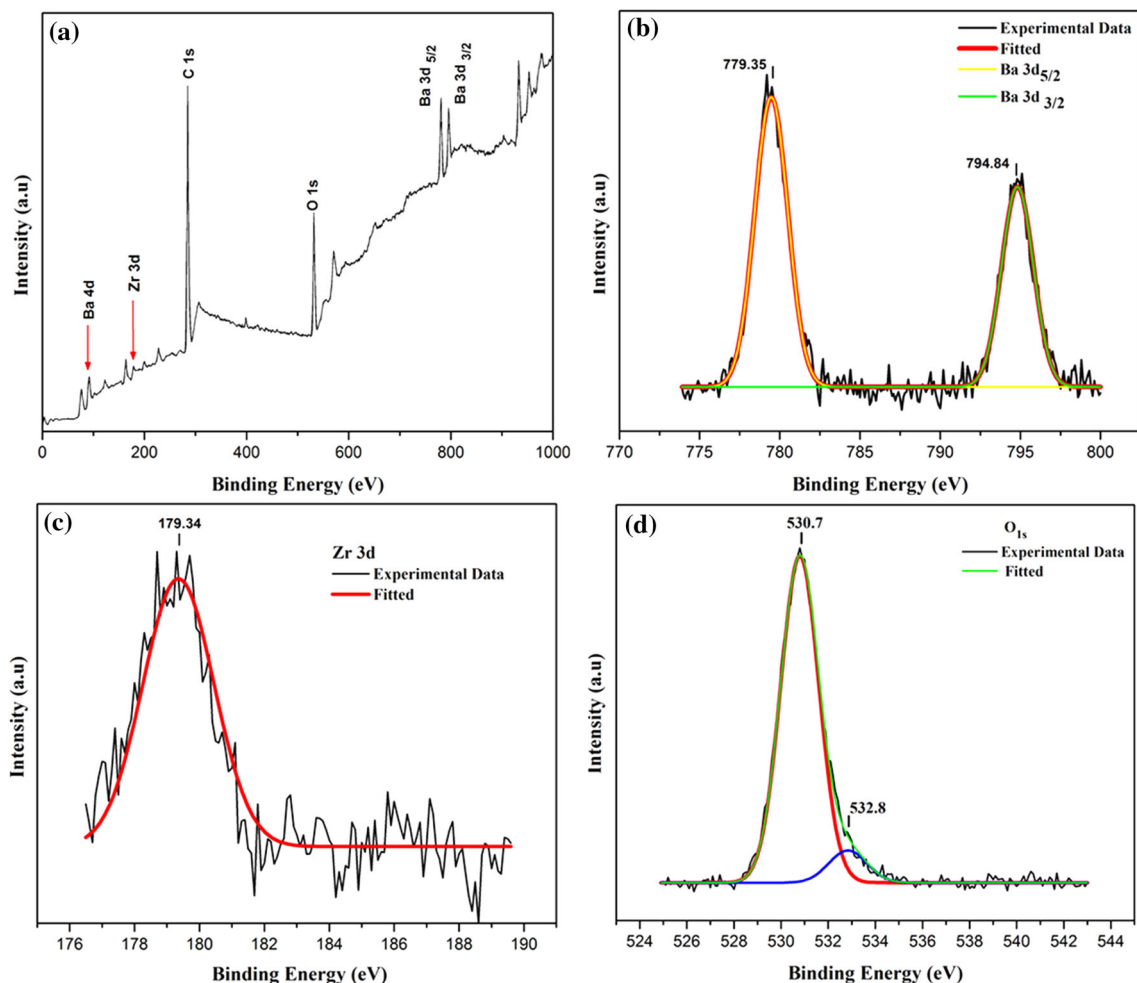
Fig. 4 XPS spectra of un-annealed $Ba_3Zr_2O_7$ thin film. **a** XPS survey spectrum; XPS core level spectra of **b** Ba 3d, **c** Zr 3d; **d** O 1s

reveals the presence of oxygen deficiencies or vacancies within the $Ba_3Zr_2O_7$ matrix as reported in literature that layered perovskite has abundant oxygen vacancies because of their loose intercalated structure [27].

The de-convoluted peak centred towards the higher binding energy side ($\sim$532.4 eV) in the present work which is associated with the presence of chemisorbed oxygen or hydroxide species within the $Ba_3Zr_2O_7$ host matrix [25, 26].

By calculating the relative area under the curves of de-convoluted peaks, the relative concentration of Ba, Zr and O was found to be 58.6, 3.46 and 37.91 %, respectively. It manifests that the film is a barium-rich film with the deficiency of zirconium and oxygen.

3.3 Morphological characterization

3.3.1 FE-SEM/EDX analysis

Figure 5 presents the surface morphology obtained using FE-SEM of the $Ba_3Zr_2O_7$ thin films un-annealed (a) and

annealed at 500° (b). The features at the surface of as-deposited thin film are of irregular-shaped micron-size particulates which are randomly oriented on the surface. The formation of these micron-size particles is attributed to boiling, splashing, exfoliation and sputtering of target [28, 29] during laser ablation process. The surface morphology of the film post-annealed at 500 °C (Fig. 5b) indicates that the thin film has best smoothness among all the deposited thin films. The surface profile of the film is better as compared to the un-annealed film. The formation of uniform film, annealed at 500 °C (Fig. 5b), having densely populated microstructure, is attributed to the high-temperature treatment due to which atoms on the surface of the films (adatoms) get diffused and the enlargement of grain occurs. This enlargement causes the improvement in the crystallinity [30] as confirmed by the XRD pattern (Fig. 2).

EDX analysis has been carried out in order to verify the composition of the deposited thin films. The EDX spectra of the film post-annealed at 500 °C are shown in Fig. 6. It confirms the presence of all the elements of the target material in the deposited thin films in an appropriate
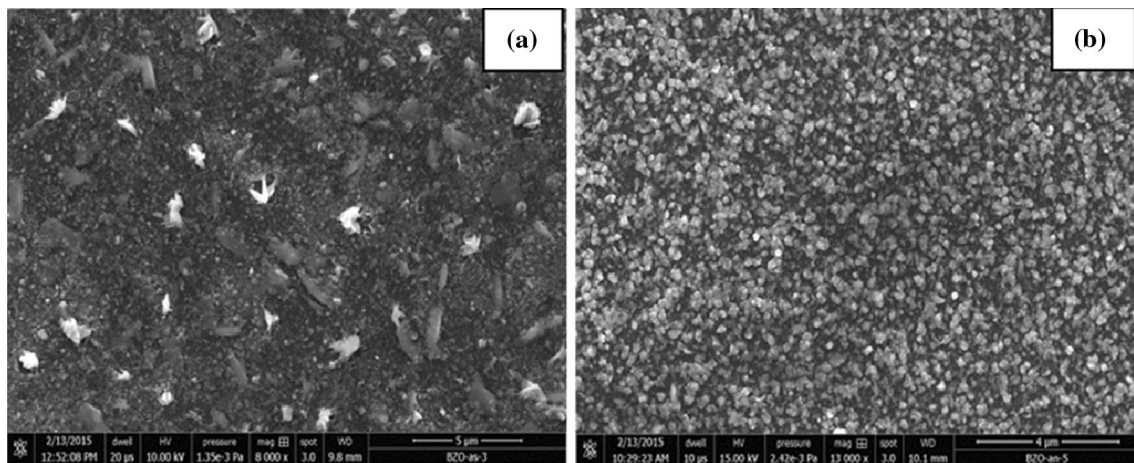
Fig. 5 FE-SEM micrographs of Ba$_3$Zr$_2$O$_7$ films deposited at 300 °C substrate temperature. **a** as-deposited, **b** annealed at 500 °C

Table 1 Composition of film as-deposited and post-annealed at 500 °C as detected by EDX analysis

Elements	As-deposited film Atomic %	Annealed film at 500 °C Atomic %
OK	6.83	6.85
SiK	88.38	88.36
ZrL	1.78	1.73
BaL	3.01	3.06

composition along with the silicon peak from the substrate. The atomic per cents of constituent elements for the film un-annealed and post-annealed at 500 °C are listed in Table 1.

3.3.2 AFM analysis

Atomic-force microscope (AFM) is used to measure the surface roughness of Ba$_3$Zr$_2$O$_7$ thin films (Fig. 7) for a scan area 5 μm × 5 μm. The AFM micrograph of un-annealed thin film is shown in Fig. 7a, while the thin films annealed at 500, 600 and 800 °C are shown in Fig. 7b–d, respectively.

The surface of the un-annealed film exhibits dense-film morphology with widely distributed particulates on the surface that grounds roughness of the film surface. The surface of film post-annealed at 500 °C is found to be the smooth with insignificant number of particulates on the surface, thus improving the surface quality of the film. Film uniformity has been reduced in the case of film post-annealed at 600 and 800 °C due to formation of larger-size particulates. The surface roughness of the un-annealed film and the films annealed at 500, 600 and 800 °C was found to be 37.87, 27.51, 51.03 and 64.84 nm, respectively. The rms roughness value for the film post-annealed at 500 °C is evidence of the improvement in smoothness as depicted by FE-SEM results. It is inferred from the AFM images
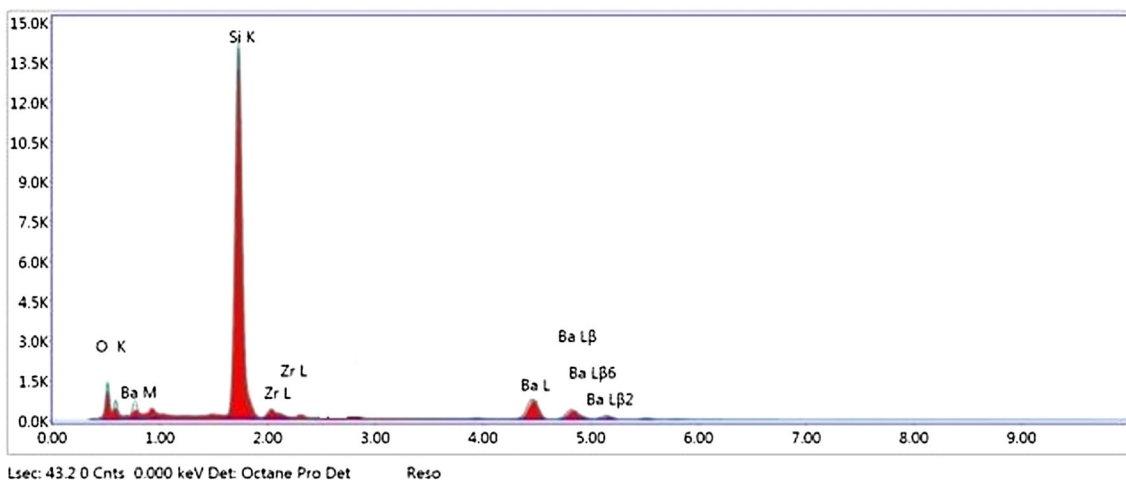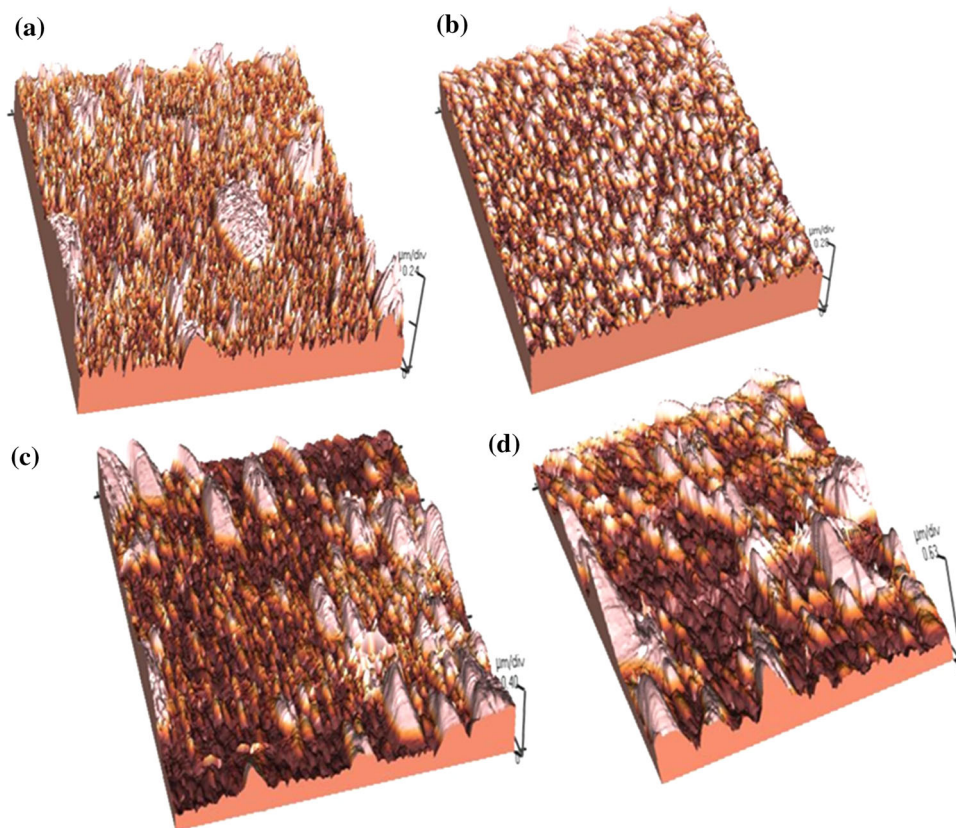

Fig. 6 EDX spectra of Ba$_3$Zr$_2$O$_7$ films post-annealed at 500 °C

Fig. 7 AFM micrograph (5 μm × 5 μm) of $Ba_3Zr_2O_7$ films deposited at 300 °C substrate temperature. **a** as-deposited, **b** Annealed at 500 °C, **c** annealed at 600 °C, **d** annealed at 800 °C

(Fig. 7b–d) that the surface roughness increases with the increase in annealing temperature (Fig. 8) due to the formation of lager particles on the surface. Hence, the rms roughness is directly dependent on annealing temperature as reported earlier [31].

3.4 Optical characterization

Optical properties are studied using spectroscopic ellipsometry (SE). It is an optical measurement technique that can be used to measure various optical constants such as refractive index (n), extinction coefficient (k), dielectric constant (ε) and optical band gap energy (E_g). The spectroscopic analysis of all $Ba_3Zr_2O_7$ thin films is performed in 500–900 nm spectral range. The experimental data are fitted to Cauchy's model. The data obtained from the SE are plotted in Fig. 9.

Variation of refractive index with respect to wavelength for all deposited film is shown in Fig. 9a. The maximum value of n is observed for the film post-annealed at 500 °C due to the better packing density and increased crystallinity of the film [21] as depicted by the XRD patterns. As far as the variation in the n with the wavelength for all the films is concerned, it is observed that refractive index of the un-annealed film remains almost constant ($n \sim 1.22$)in the wavelength range of 500–900 nm, whereas there is a slight
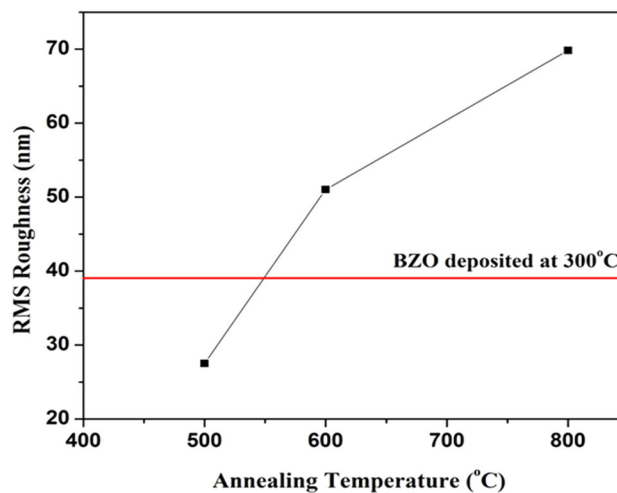
Fig. 8 Variation of RMS roughness with annealing temperature

increase in $n(n \sim 1.24)$ in the wavelength range of 610–760 nm. The refractive index of the film post-annealed at 500 °C also remains almost constant ($n \sim 1.81$) in the visible-to-NIR region of the spectrum. The figure indicates the decrease in the value of n with increasing wavelength for both the films post-annealed at 600 and 800 °C from visible-to-NIR region of the spectrum. The extinction coefficient in Fig. 9b shows a similar trend as that of refractive index, i.e.
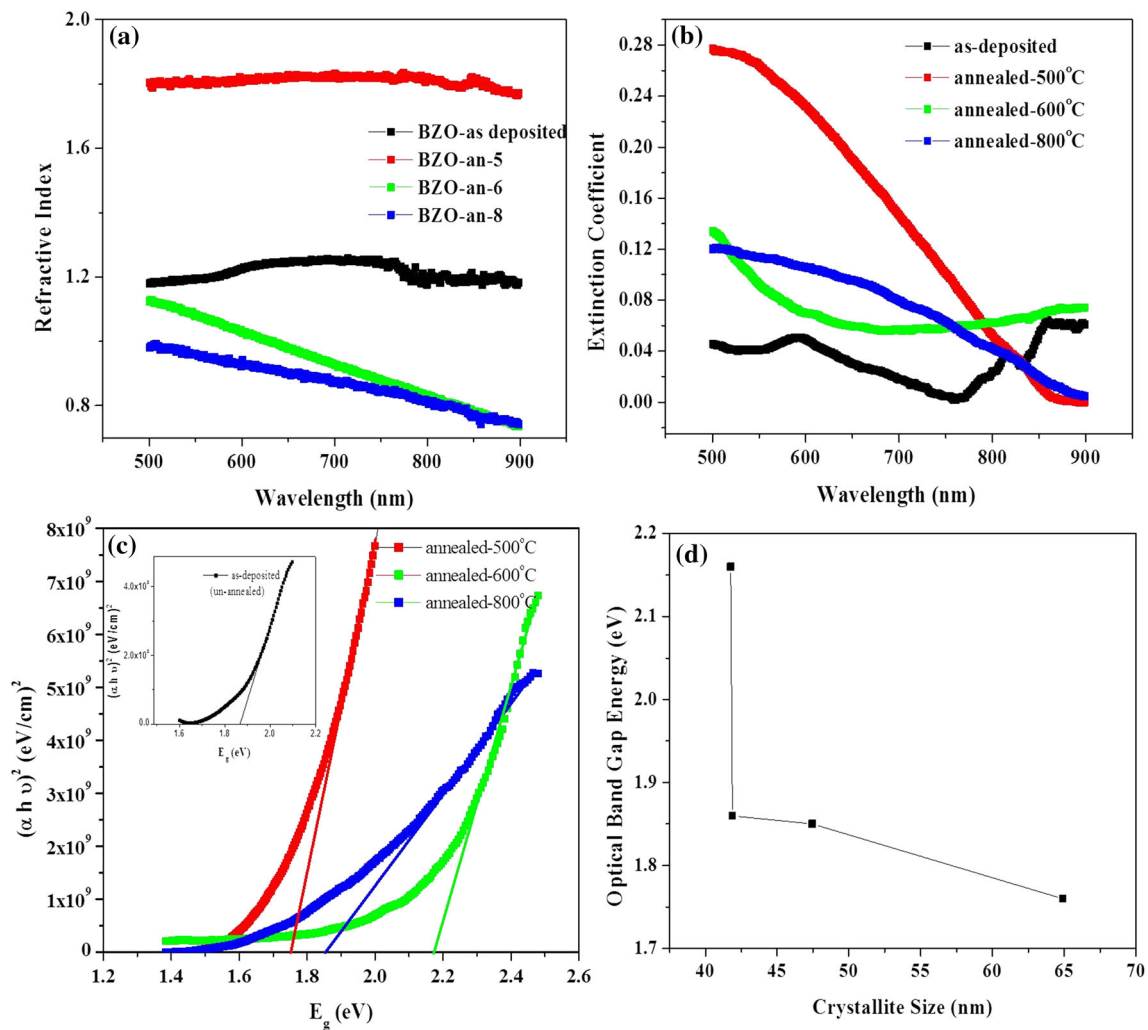
Fig. 9 Optical constants of all thin films **a** n, **b** k, **c** $(\alpha h\nu)^2$ verses $h\nu$, and **d** variation of optical band gap energy with the crystallite size

the maximum value of extinction coefficients obtained for the film post-annealed at 500 °C. The film exhibits a decreasing trend in the extinction coefficient with the increase in the wavelength. The un-annealed film shows a rise and fall in the value of extinction coefficient with the increasing wavelength (Fig. 9b). There is a decrease in the value of k from 591 to 760 nm, whereas it increases in the IR region up to 900 nm. The films post-annealed at 600 and 800 °C demonstrate a decrease in the value of k with the increasing wavelength from visible-to-NIR region. The reason for this change in the k with the wavelength is a measure of the change in the absorbance [32].

The optical band gap energy of the deposited films is calculated by using the Tauc's relation [29]:

$$\alpha h\nu = M\left[h\nu - E_g\right]^r \tag{1}$$

where M is the constant of materials, and r is an index which depends on the type of the electronic transitions

responsible for the optical absorption. The value of r for allowed direct transition is 1/2 and for indirect transition is 2. The allowed direct band gap energy can be evaluated from the intercept of the straight lines on the energy axis at $(\alpha h\nu)^2 = 0$.

The Tauc's plots for the films annealed at 500, 600 and 800 °C are shown in Fig. 9c while the Tauc's plot of un-annealed thin film is exhibited in the inset. The optical band gap energy of as-deposited thin film is found to be 1.86 eV. While the optical band gap energies of the films annealed at 500, 600 and 800 °C are 1.75, 2.15 and 1.80 eV, respectively. There has been a decrease in the optical band gap energy in the case of deposited film of Ba$_3$Zr$_2$O$_7$ in comparison with the target material (5.4 eV for cubic BaZrO$_3$ [33]) which is due to the change of BaZrO$_3$ phase into the disordered clusters of Ba$_3$Zr$_2$O$_7$ phase having defects including oxygen vacancies in deposited film [2]. It has also been reported that the layered perovskite structures (like

$Ba_3Zr_2O_7$) have smaller band gap values than the parent perovskite oxides (ABO_3) [34]. Figure 9d reveals the variation of optical band gap energy with the crystallites size of all thin films. It is evident that the films with larger crystallites have the lower value of optical band gap energy. It is attributed to the decrease in the strain and dislocation density with the increase in the crystalline size. As the crystal grows, the grain boundaries are relaxed and eliminated which lead to the rearrangement of atoms in such a way that strain energy decreases [35, 36].

4 Conclusion

In present research work, a new phase with the composition $Ba_3Zr_2O_7$ has been grown as thin films on Si (0 0 1) substrate by PLD technique. There is formation of tetragonal $Ba_3Zr_2O_7$ (0 0 8) phase in all deposited films regardless of the annealing temperature. However, the film post-annealed at 500 °C has the maximum growth of the $Ba_3Zr_2O_7$ (0 0 8) phase. Further increase in the annealing temperature leads to the decreased growth of the phase. The XPS results show that Ba, Zr and O exist mainly in the form of $Ba_3Zr_2O_7$ Ruddlesden–Popper-type perovskite structure. The uniformity and smoothness of the film are found to be maximum at annealing temperature of 500 °C. As far as the optical parameters of the films are concerned, the refractive index and extinction coefficient of the film annealed at 500 °C carry maximum values, whereas the optical band gap energy has the minimum value.

It is inferred that the PLD is a suitable technique to grow tetragonal $Ba_3Zr_2O_7$ (0 0 8) thin films. Furthermore, the 500 °C annealing temperature is the optimum temperature to grow $Ba_3Zr_2O_7$ tetragonal phase with best crystallinity and minimum optical band gap energy. These properties make the thin films to be potential candidates for the optoelectronic devices.

References

1. J. Wu, *Defect chemistry and proton conductivity in Ba-based perovskites* [PhD thesis]. California: California Institute of Technology, Pasadena, 2005
2. M.F.C. Gurgel, M.L. Moreira, E.C. Paris, J.W.M. Espinosa, P.S. Pizani, J.A. Varela, E. Longo, Int. J. Quantum Chem. **111**, 694–701 (2011)
3. F.A. Mir, M. Ikram, R. Kumar, Phase Transit **84**, 167–178 (2011)
4. Y. Kitano, T. Matsui, N. Fujimura, K. Morii, T. Ito, J. Cryst. Growth **243**, 164–169 (2002)
5. G. Rog, M.M. Bucko, A. Kozlowska-Rog, J. Chem. Thermodyn. **40**, 21–24 (2008)
6. A. Molak, M. Pawełczyk, J. Kubacki, K. Szot, Phase Transit **82**, 662–682 (2009)
7. A. Chroneos, R.V. Vovk, I.L. Goulatis, L.I. Goulatis, J. Alloys Compd. **494**, 190–195 (2010)
8. W. Tian, J.H. Haeni, D.G. Schlom, E. Hutchinson, B.L. Sheu, M.M. Rosario, P. Schiffer, Y. Liu, M.A. Zurbuchen, X.Q. Pan, Appl. Phys. Lett. **90**, 022507 (2007)
9. A.H. Reshak, S. Auluck, I. Kityk, Jpn. J. Appl. Phys. **47**, 5516–5520 (2008)
10. L.S. Cavalcante et al., Opt. Commun. **281**, 3715–3720 (2008)
11. D. Neiner, *New Ruddlesden–Popper perovskites obtained by topochemical methods* [PhD Thesis]. USA: University of New Orleans, 2005
12. K.S. Aleksandrov, J. Bartolom, Phase Transit. **74**, 255–335 (2001)
13. D. W. Bäuerle, *Laser Processing and Chemistry*, (Springer, Berlin, Heidelberg, 2011)
14. T. Ohnishi, K. Takada, Appl. Phys. Express **4**, 025501 (2011)
15. A. Usman, M.S. Rafique, M. Khaleeq-ur-Rahman, K. Siraj, S. Anjum, H. Latif, T.M. Khan, M. Mehmood, Mater. Chem. Phys. **126**, 649–654 (2011)
16. D. Singh, R. Singh, J. Chem. Sci. **122**, 807–811 (2010)
17. B.D. Cullity, *Elements of X-Ray Diffraction,* (Addison-Wesley Publishing Company, USA, 1956)
18. J.H. Haeni, C.D. Theis, D.G. Schlom, W. Tian, X.Q. Pan, H. Chang, I. Takeuchi, X.D. Xiang, Appl. Phys. Lett. **78**, 3292–3294 (2001)
19. H. Latif, M.S. Rafique, M. Khaleeq-ur-Rahaman, R.S. Rawat, A. Sattar, S. Naseem, P. Lee, Appl. Surf. Sci. **254**, 7505–7511 (2008)
20. S. Kose, F. Atay, V. Bilgin, I. Akyuz, Mater. Chem. Phys. **111**, 351–358 (2008)
21. T. Supasai, S. Dangtip, P. Learngarunsri, N. Boonyopakorn, A. Wisitsoraat, S.K. Hodak, Appl. Surf. Sci. **256**, 4462–4467 (2010)
22. I. Marozau, *Pulsed laser deposition and characterisation of perovskite-type oxynitride thin films* [PhD thesis], Belarusian State University, Republic of Belarus, 2009
23. L.L. Jiang, X.G. Tang, S.J. Kuang, X.F. Xiong, Appl. Surf. Sci. **255**, 8913–8916 (2009)
24. H. Li, J.-I.J. Choi, W. Mayr-Schmölzer, C. Weilach, C. Rameshan, F. Mittendorfer, J. Redinger, M. Schmid, G. Rupprechter, J. Phys. Chem. C **119**, 2462–2470 (2015). doi:10.1021/jp5100846
25. U. Ilyas, T.L. Tan, P. Lee, R.V. Ramanujan, F. Li, S. Zhang, R. Chen, H.D. Sun, R.S. Rawat, J. Mag. Mag. Mater. **344**, 171–175 (2013)
26. K.M. Wong, Y. Fang, A. Devaux, L. Wen, J. Huang, L. De Cola, Y. Lei, Nanoscale **3**, 4830 (2011)
27. X. Du, G. Zou, X. Wang, Catal. Surv. Asia **19**, 17–24 (2015). doi:10.1007/s10563-014-9178-7
28. S. Anjum, M.S. Rafique, M. Khaleeq-ur-Rahman, K. Siraj, A. Usman, H. Latif, K.A. Bhatti, S. Hussain, S. Naseem, Vacuum **85**, 126–130 (2010)
29. D.B. Chrisey, G.K. Hubler (eds.), *Pulsed Laser Deposition of Thin Films* (Wiley, New York, 1994)
30. F. Shi, C. Cui, Inorg. Mater. **46**, 565–569 (2010)
31. X. X. Chen, M. Sorenson, C. Butler, L. Rieth, M. S. Miller, F. Solzbacher, Proceedings of Material Research Society Symposium 1010, 1010-V03-01 (2007), Materials Research Society, USA
32. M.Y. Nadeem, W. Ahmed, Turk. J. Phys. **24**, 651–659 (2000)
33. G. Łupina et al., Appl. Phys. Lett. **94**, 152903 (2009)

34. I.E. Castelli, J.M. Garcia-Lastra, F. Huser, K.S. Thygesen, K.W. Jacobsen, New J. Phys. **15**, 105026 (2013)

35. Z.R. Khan, M. Zulfequar, M.S. Khan, Chalcogenide Lett. **7**, 431–438 (2010)

36. U. Parihar, N. Padha, J.R. Ray, M.S. Desai, C.J. Panchal, P.K. Mehta, I.V. Cheshko, I.Y. Protsenko, Proc. Int. Conf. Nanomater. Appl. Prop. **2**, 6 (2013)